ELSEVIER

## Contents lists available at ScienceDirect

# Acta Biomaterialia

journal homepage: www.elsevier.com/locate/actbio



# Full length article

# Controllable biodegradation and enhanced osseointegration of ZrO<sub>2</sub>-nanofilm coated Zn-Li alloy: *In vitro* and *in vivo* studies



Wei Yuan<sup>a,1</sup>, Dandan Xia<sup>a,1</sup>, Yufeng Zheng<sup>a,b,\*</sup>, Xiangmei Liu<sup>c</sup>, Shuilin Wu<sup>d,\*</sup>, Bo Li<sup>e</sup>, Yong Han<sup>e,\*</sup>, Zhaojun Jia<sup>f</sup>, Donghui Zhu<sup>g</sup>, Liqun Ruan<sup>h</sup>, Kazuki Takashima<sup>i</sup>, Yunsong Liu<sup>j,k,\*</sup>, Yongsheng Zhou<sup>j,k</sup>

- <sup>a</sup> Department of Materials Science and Engineering, College of Engineering, Peking University, Beijing 100871, China
- b International Research Organization for Advanced Science and Technology, Kumamoto University, 2-39-1 Kurokami, Chuo-Ku, Kumamoto 860-8555, Japan
- <sup>c</sup> Ministry-of-Education Key Laboratory for the Green Preparation and Application of Functional Materials, Hubei Key Laboratory of Polymer Materials, School of Materials Science & Engineering, Hubei University, Wuhan, 430062, China
- <sup>d</sup> School of Materials Science & Engineering, The Key Laboratory of Advanced Ceramics and Machining Technology by the Ministry of Education of China, Tianjin University, Tianjin, 300072, China
- eState Key Laboratory for Mechanical Behavior of Materials, Xi'an Jiaotong University, Xi'an 710049, China
- <sup>f</sup> Department of Chemistry and Chemical Biology, Rutgers University, Piscataway, NJ 08854, USA
- <sup>g</sup> Department of Biomedical Engineering, Institute for Engineering-Driven Medicine, College of Engineering and Applied Sciences, Renaissance School of Medicine, Stony Brook University, 100 Nicolls Rd, Stony Brook, NY 11794, USA
- <sup>h</sup> Department of Mechanical Systems Engineering, Graduate School of Science and Technology, Kumamoto University, Kurokami 2-39-1, Kumamoto-shi 860-8555, Japan
- <sup>1</sup>Department of Materials Science and Engineering, Faculty of Engineering, Kumamoto University, 2-39-1 Kurokami, Kumamoto 860-8555, Japan
- Department of Prosthodontics, Peking University School and Hospital of Stomatology, Beijing 100081, China
- <sup>k</sup> National Engineering Laboratory for Digital and Material Technology of Stomatology, National Clinical Research Center for Oral Diseases, Beijing Key Laboratory of Digital Stomatology, Beijing 100081, China

# ARTICLE INFO

Article history: Received 29 October 2019 Revised 11 January 2020 Accepted 15 January 2020 Available online 20 January 2020

Keywords: Zn-Li alloy Zirconia nanofilm Atomic layer deposition Biodegradation Biocompatibility Orthopedic implants

# ABSTRACT

Zinc and its alloys have emerged as a new research direction of biodegradable metals (BMs) due to the significant physiological functions of Zn<sup>2+</sup> ions in human body. However, low inhibitory concentration threshold value to cause cytotoxicity by Zn<sup>2+</sup> ions during *in vitro* study and delayed osseointegration *in vivo* are two key flaws for the bulk Zn-based BMs. To combat these issues, we constructed a barrier layer of ZrO<sub>2</sub> nanofilm on the surface of Zn-0.1(wt.%) Li alloy via atomic layer deposition (ALD). A decreased release of Zn<sup>2+</sup> ions accompanied with accelerated release of Li<sup>+</sup> ions was observed on account of galvanic coupling between the coating compositions and Zn-0.1Li alloy substrate. Cytocompatibility assay reflected that ZrO<sub>2</sub> nanofilm coated Zn-0.1Li alloy exhibited improved cell adhesion and viability. Histological analysis also demonstrated better *in vivo* osseointegration for the ZrO<sub>2</sub> nanofilm coated Zn-0.1Li alloy. Hence, the present study elucidated that the ALD of ZrO<sub>2</sub> nanofilm on Zn-based BMs can effectively promote osseointegration and control their biodegradation behavior.

## **Statement of Significance**

Zn-Li binary alloy was reported recently to be the promising biodegradable metals with ultimate tensile strength over 500 MPa, yet the low inhibitory concentration threshold value to cause cytotoxicity by  $\rm Zn^{2+}$  ions is the obstacle needed to be overcome. As a pilot study, a systematic investigation on the  $\rm ZrO_2$  nanofilm coated Zn-Li alloy, prepared by atomic layer deposition (ALD) technique, was conducted in the present study, which involved in the formation process, *in vitro* and *in vivo* degradation behavior as well as biocompatibility evaluation. We found a controllable corrosion rate and better *in vivo* osseointegration can be achieved by  $\rm ZrO_2$  nanofilm coating on  $\rm Zn$ -Li alloy, which provides new insight into the surface modification on biodegradable Zn alloys for usage within bone.

© 2020 Acta Materialia Inc. Published by Elsevier Ltd. All rights reserved.

<sup>\*</sup> Corresponding authors.

E-mail addresses: yfzheng@pku.edu.cn (Y. Zheng), shuilinwu@tju.edu.cn (S. Wu), hanyong@xjtu.edu.cn (Y. Han), liuyunsong@hsc.pku.edu.cn (Y. Liu).

 $<sup>^{\</sup>rm 1}$  Wei Yuan and Dandan Xia contributed equally to this study.

## 1. Introduction

Biodegradable metals (BMs) have spurred great interest over the past decades. In contrast to permanent metallic biomaterials such as stainless steel, titanium and titanium alloys, BMs are expected to gradually corrode in physiological environment after fulfilling the mission of assisting tissue healing, and the degradation products can be metabolized by human body without causing any adverse host response [1]. In this regard, the biocorrosion rate should ideally be neither too low or too high. Recently Zn and its alloys had emerged as a potent substitution to the existing Mg and Fe-based BMs given its intermediate corrosion potential and more appropriate corrosion rates [2]. In addition, Zn, as the second most abundant metal element in human body, also plays a significant role in eliciting numerous physiological functions [3,4]. Element Zn has proven to participate in bone formation by promoting bone growth, mineralization, and preserving bone mass [5]. Nevertheless, concerns remain about the local and systemic toxicity of the degradation products of Zn-based BMs. The pure Zn extracts exhibited a significant cytotoxicity to osteoblasts in vitro [6]. Direct culture of osteoblasts on pure Zn surface also indicated low cell viability [7,8]. Meanwhile, poor osseointegration was observed due to a locally high Zn ion when implanted into the rat femur condyle [9]. Zn can be beneficial or harmful to osteoblasts. The low Zn<sup>2+</sup> concentrations improve cell viability, whilst the opposite is true at high concentrations [10]. Since the concentration of the ionic degradation products is directly related to the corrosion rate, it is essential to develop Zn-based materials with appropriate corrosion behaviors.

ZrO<sub>2</sub> has been amply used in dentistry and orthopedics due to its favorable mechanical strength and biocompatibility [11]. Recent studies have demonstrated that ZrO<sub>2</sub> has low cytotoxicity *in vitro* and good biocompatibility *in vivo* [12]. ZrO<sub>2</sub> coating can induce aggregation of apatite in simulated body fluid and show beneficial effects on the osteoblast adhesion and proliferation [13,14]. In addition, an inhibitory effect of ZrO<sub>2</sub> on bacterial colonization was observed [15]. To improve the anti-wear and/or anti-corrosion performances, ZrO<sub>2</sub> films have been deposited onto different substrates by variety of methods, including atomic layer deposition (ALD), plasma immersion ion implantation and deposition [16], plasma electrolytic oxidation [17], plasma spraying [18], sol-gel [19], etc.

In particular, ALD has risen as a powerful tool in nanofabrication such as semiconductors [20], showing obvious advantages in conformality and precise control over material thickness and composition [21]. ALD is capable of depositing homogeneous conformal films on either flat surface or complex structures with film thickness at the angstrom level [22,23]. Recently, various metallic oxides have been successfully applied as coating materials onto biomaterials via ALD. For example, ZrO<sub>2</sub> and TiO<sub>2</sub> nanofilms have been thus deposited on Mg alloys as a physical barrier against fast biocorrosion for superior biocompatibility [23,24]. Expectedly, the deposition of well-defined ZrO<sub>2</sub> films via ALD should afford elegant control over the corrosion behaviors of Zn-based RMs

As for the orthopedic application, the mechanical strength of pure Zn is not strong enough to meet the clinical requirements [5,25]. The significant solubility of Li in Zn renders Zn-Li alloys as a promising age-hardenable systems. Zhao et al. [26] incorporated 0.1 wt.% of Li into Zn and found that the tensile strength increased from 116  $\pm$  13 MPa to 274  $\pm$  61 MPa. Dai et al. [27] also demonstrated that alloying with 0.5 wt.% Li improved the tensile strength and elongation remarkably compared with pure Zn. In the present research, a layer of ZrO2 nanofilm was constructed on top of Zn-0.1Li alloy (ZL) to control the corrosion rate of the substrate. The micro/nano structure, *in vitro* corrosion behavior, cytocompatibility

and *in vivo* biocompatibility were investigated to assess the feasibility of the ZrO<sub>2</sub> coated Zn-based BMs for orthopedic application.

#### 2. Materials and methods

#### 2.1. Material preparation

Zn-0.1Li (wt.%) binary alloy ingots were prepared from pure Zn (99.99%) ingot and pure Li (99.95%) ingot in a graphite crucible at 480 °C. Then the ingots were extruded at 280 °C with an extrusion ratio of 33.64. For *in vitro* studies, samples with a dimension of  $\phi$ 10 mm  $\times$  2 mm were cut from the extruded rods. For *in vivo* studies,  $\phi$ 2 mm  $\times$  6 mm cylinders were used. Prior to use, each sample was mechanically polished to 2000 grit by SiC papers and then ultrasonically rinsed in acetone, absolute ethanol and distilled water, followed by drying in open air.

#### 2.2. Atomic layer deposition

For ZrO<sub>2</sub> deposition, a commercial ALD reactor (F-100-41, MNT Micro and Nanotech Co., LTD, Wuxi, China) was employed. The Tetrakis (dimethylamino) zirconium (TDMAZ) and deionized water were used as Zr and O precursors, respectively. The Zr and O precursors were heated to 120 °C, and 35 °C, respectively, followed by alternate deposition cycles using the two precursors. A series of ZrO<sub>2</sub> coatings were constructed at varying deposition cycles: 100, 300 and 500, which were denoted as ZrO<sub>2</sub>-100, ZrO<sub>2</sub>-300 and ZrO<sub>2</sub>-500, respectively.

## 2.3. Surface characterization

Surface morphologies and element compositions were investigated via scanning electron microscopy (S-4800 Emission Scanning electron microscopy, Hitachi, Japan) equipped with Energy Dispersive X-ray spectrometer. The surface phase analysis was conducted by X-ray diffraction (XRD, Rigaku DMAX 2400, Japan) using Cu-K $\alpha$  radiation at a scan rate of 4°/min between  $2\theta$  of  $10^\circ$  and  $90^\circ$  at 40 kV and 100 mA. Auger electron spectroscopy (AES, PHI 700, ULVAC-PHI, Japan) measurements were carried out to identify the depth profile of element distribution. X-ray photoelectron spectroscope (XPS, Axis Ultra, Kratos Analytical, Britain) was applied to determine the surface chemical composition.

#### 2.4. Electrochemical evaluations

A classical three-electrode system was adopted to carry out the electrochemical test with a platinum electrode as counter electrode, a saturated calomel electrode as reference electrode and the test sample with an exposed surface of 5 mm in diameter as working electrode. The test process proceeded in Hanks' solution (NaCl  $8.00 \text{ g L}^{-1}$ , KCl  $0.40 \text{ g L}^{-1}$ , CaCl<sub>2</sub>  $0.14 \text{ g L}^{-1}$ , NaHCO<sub>3</sub>  $0.35 \text{ g L}^{-1}$ , glucose 1.00 g L<sup>-1</sup>, MgCl<sub>2</sub>·6H<sub>2</sub>O 0.10 g L<sup>-1</sup>, MgSO<sub>4</sub>·7H<sub>2</sub>O 0.06 g L<sup>-1</sup>,  $Na_2HPO_4\cdot 12H_2O\ 0.06\ g\ L^{-1}$  and  $KH_2PO_4\ 0.06\ g\ L^{-1}$ , pH 7.4) at ambient temperature using an electrochemical station (Autolab, Metrohm, Switzerland). Each sample underwent an open circuit potential (OCP) monitor of 5400 s. Electrochemical impedance spectroscopy measurements were performed by applying 10 mV perturbation with frequency ranging from  $10^5$  Hz to  $10^{-2}$  Hz. Afterwards, the potentiodynamic polarization curves were measured at a scanning rate of 1 mV/s. Electrochemical parameters including corrosion potential, corrosion current density and corrosion rate were estimated from polarization plots via Tafel analysis.

## 2.5. Immersion tests

In vitro immersion test was conducted to evaluate the long-term corrosion behavior according to ASTM G31-72. The samples

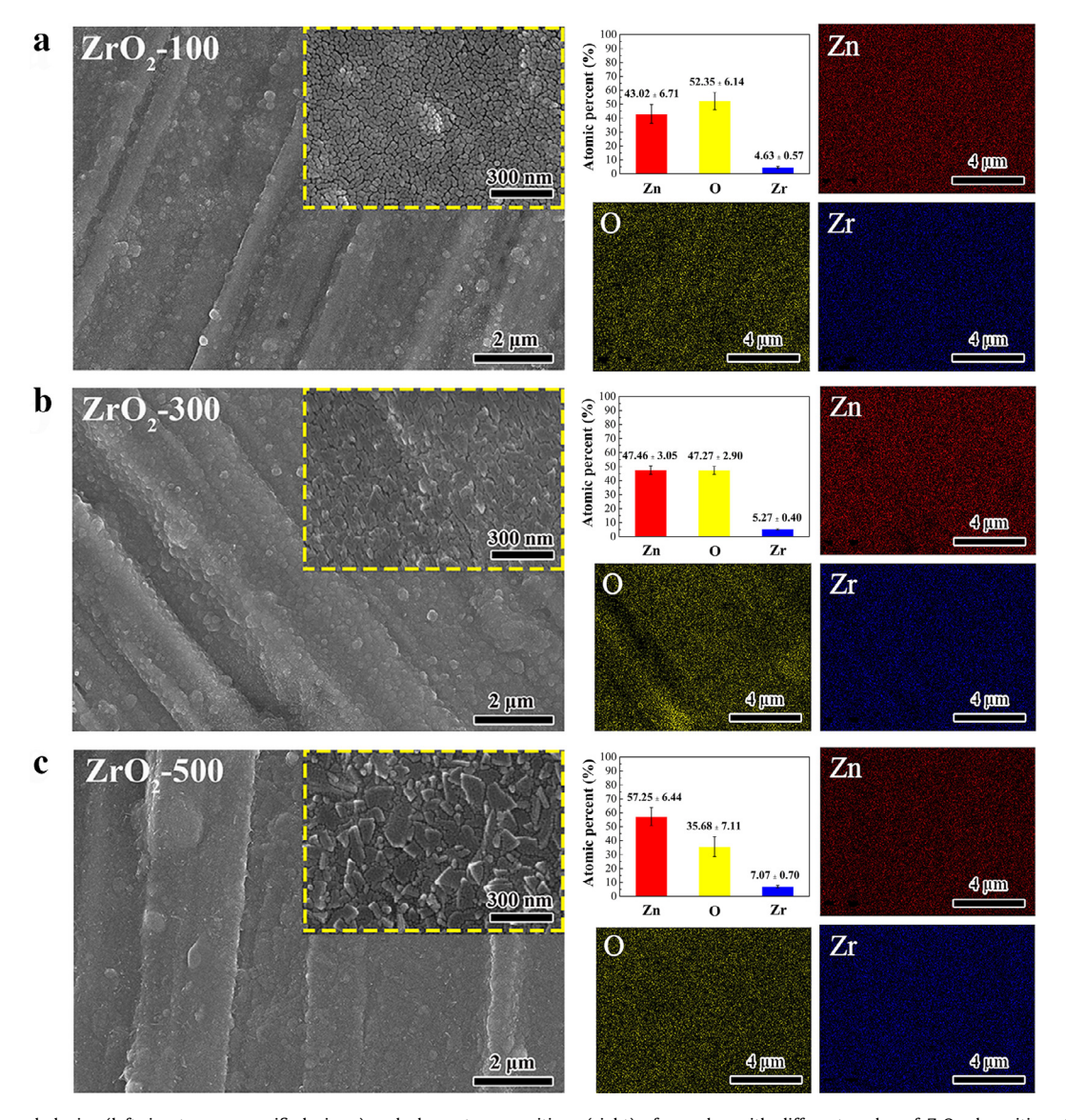


Fig. 1. Surface morphologies (left, insets are magnified views) and element compositions (right) of samples with different cycles of ZrO<sub>2</sub> deposition: (a) ZrO<sub>2</sub>-100, (b) ZrO<sub>2</sub>-300, and (c) ZrO<sub>2</sub>-500.

were immersed in Hanks' solution at 37 °C for 28 days with an exposure ratio of 20 ml per 1 cm<sup>2</sup>. The pH values were determined during immersion. At the end of immersion, samples were collected, washed with deionized water and dried in air. SEM and XRD were employed to investigate the change in surface morphology and chemical composition. The Zn ion concentration in Hanks' solution was characterized by inductively coupled plasma atomic emission spectrometry (ICP).

#### 2.6. Cytocompatibility

Mouse osteoblast-like cells (MC3T3-E1) were employed to evaluate the cytocompatibility according to ISO 10993-5: 2009. MC3T3-E1 cells were cultured in Dulbecco's modified Eagle's medium (DMEM) containing 10% fetal bovine serum (FBS), 100 U/mL penicillin and 100  $\mu$ g/mg streptomycin in a humidified atmosphere of 5% CO<sub>2</sub> at 37 °C. Prior to use, each side of the sample was subjected to UV radiation for at least 1 h. Material extracts were collected by incubating the samples in DMEM cell culture medium with an extraction ratio of 1.25 ml per 1 cm<sup>2</sup> under standard cell culture condition for 24 h. The average ion

concentrations of the mixed extract of at least 3 samples were determined by ICP. The cell culture medium supplemented with and without 10% dimethylsulfoxide (DMSO) was employed as positive and negative control, respectively.

In terms of cell viability assay, 100  $\mu$ l cell suspension was seeded into the 96-well cell culture plates at a cell density of 3  $\times$  10<sup>4</sup> cells/ml. Cell culture mediums was replaced with material extracts after 24 h of incubation for cell adhesion. Then the cells were incubated for 1, 3 and 5 days, respectively. At the end of each time point, cell culture medium with 10% Cell Counting Kit-8 (CCK8, Dojindo, Japan) substituted the material extracts and incubated at 37 °C for 1 h. The spectrophotometric absorbance of each group was determined via a microplate reader (Bio-RAD680) at a wavelength of 450 nm. At least five duplicates were employed for the cell viability assay.

In the direct cell experiments, cells suspension at a cell density of the  $5\times 10^4$  cell/ml was seeded on the surface of samples and incubated for 24 h to allow cell adhesion and spreading. Thereafter, cells were fixed by 4% (w/v) paraformaldehyde for 10 min, followed by permeabilization with 0.1% Triton for 7 min. Subsequently, 1.0% (v/v) FITC-phalloidin dye was employed to stain

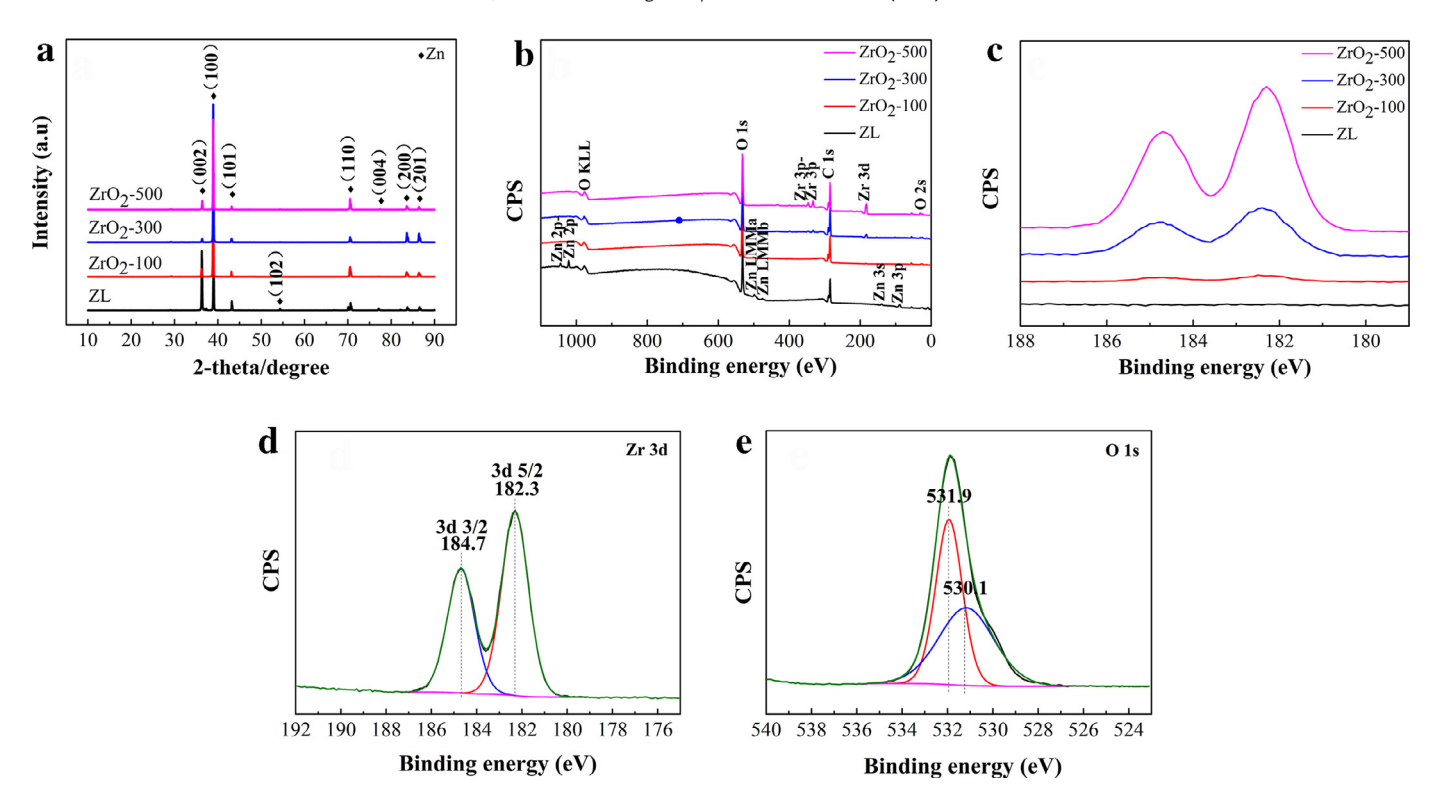


Fig. 2. Chemical composition analysis: (a) XRD patterns; (b) XPS wide-scan spectra; (c-e) High-resolution XPS spectra of Zr 3d (c, d; d is a fitted spectrum for ZrO<sub>2</sub>-500) and O 1s (e, fitted spectrum for ZrO<sub>2</sub>-500).

the microfilament for 30 min at room temperature. 1 mg/ml DAPI for nuclei was added and incubated for 10 min at 37 °C. The cell morphology was investigated by LSCM (laser scanning confocal microscope, Nikon ALR-SI).

## 2.7. Animal test

All the animal procedures and experiments were approved by the Ethics Committee, Peking University Health Science Center, Beijing, China (LA2016305). The animal experiments were carried out following the protocol formulated by the Experimental Animal Ethics Branch. Eighteen ten-week old male Sprague-Dawley (SD) rats were randomized into two groups: ZL and ZrO<sub>2</sub>-500. All rats were anesthetized by pentobarbital sodium (50 mg/kg) before surgery. All samples were implanted into a drilled bone tunnel (2 mm in diameter and 6 mm in height) in the femur condyle. A total of 36 samples were implanted. Postoperatively, all rats were raised in an environmentally controlled animal care house. Rats were sacrificed by euthanasia at 4, 8 and 12 weeks after implantation. The rat femurs, hearts, lives, spleens, lungs and kidneys were harvested and fixed in 10% neutral formalin buffer for 24 h at room temperature. At each time point, a total number of twelve femurs were harvested.

Half of the femur samples were rinsed in water for 24 h, dehydrated with gradient dehydration from 70% to absolute ethanol, and embedded in polymethylmetacrylate (PMMA). Subsequently, the embedded specimens were sectioned into 200  $\mu m$  thick sections using a EXAKT 300CP saw microtome (Leica, Hamburg, Germany). The sections were then grounded and polished to 20  $\mu m$ , followed by staining with methylene-blue/acid fuchsin staining for histological examination.

The rest of femur samples were decalcified in 10% EDTA solution (pH 7.4) at room temperature for 6 weeks. After complete decalcification, dehydration and transparency, the femurs were embedded in paraffin and sliced into 5  $\mu$ m thick slices using

a microtome. The fixed organ samples (hearts, lives, spleens, lungs and kidneys) were embedded in paraffin and 2–3 µm thick sections were prepared. The femurs samples were stained with hematoxylin-eosin (H&E) staining and Masson's trichrome staining for histological studies. The organs samples were stained with H&E staining. Images of the stained sections were obtained using an optical microscope (BX51, Olympus, Japan).

## 2.8. Statistical analysis

SPSS 18.0 (SPSS Inc., Chicago, USA) was utilized to conduct the statistical analysis. One-way analysis of variance (ANOVA) was employed to analyze the statistical significance followed by Tukey's post hoc tests. The P < 0.05 was considered statistically significant.

### 3. Results

# 3.1. Surface morphology and composition

Fig. 1 depicts the surface morphologies and element compositions of Zn-0.1Li alloy samples with different cycles of ZrO<sub>2</sub> deposition. As seen in Fig. 1a, ZrO<sub>2</sub> nanoparticles were homogenously distributed on the surface. Enlarged ZrO<sub>2</sub> nanoparticles were observed with increasing deposition cycles, resulting in thicker and denser ZrO<sub>2</sub> nanofilms (Fig. 1b-c). Meanwhile, The EDS mapping also indicated the successful deposition of ZrO<sub>2</sub> on the surface. Quantitatively, the proportion of Zr augmented over the deposition cycle (4.63  $\pm$  0.57% for 100 cycles, 5.27  $\pm$  0.40% for 300 cycles and 7.70  $\pm$  0.70% for 500 cycles).

The phase component of Zn-0.1Li alloy samples with and without  $ZrO_2$  deposition are displayed in Fig. 2a. The crystallized phase of  $ZrO_2$  was not detected, leading the authors to hypothesize that the as-deposited  $ZrO_2$  coatings may exist in an amorphous state with TDMAZ as zirconium source at low reaction temperature [28,29]. Both XPS survey (Fig. 2b) and high-resolution spectra of

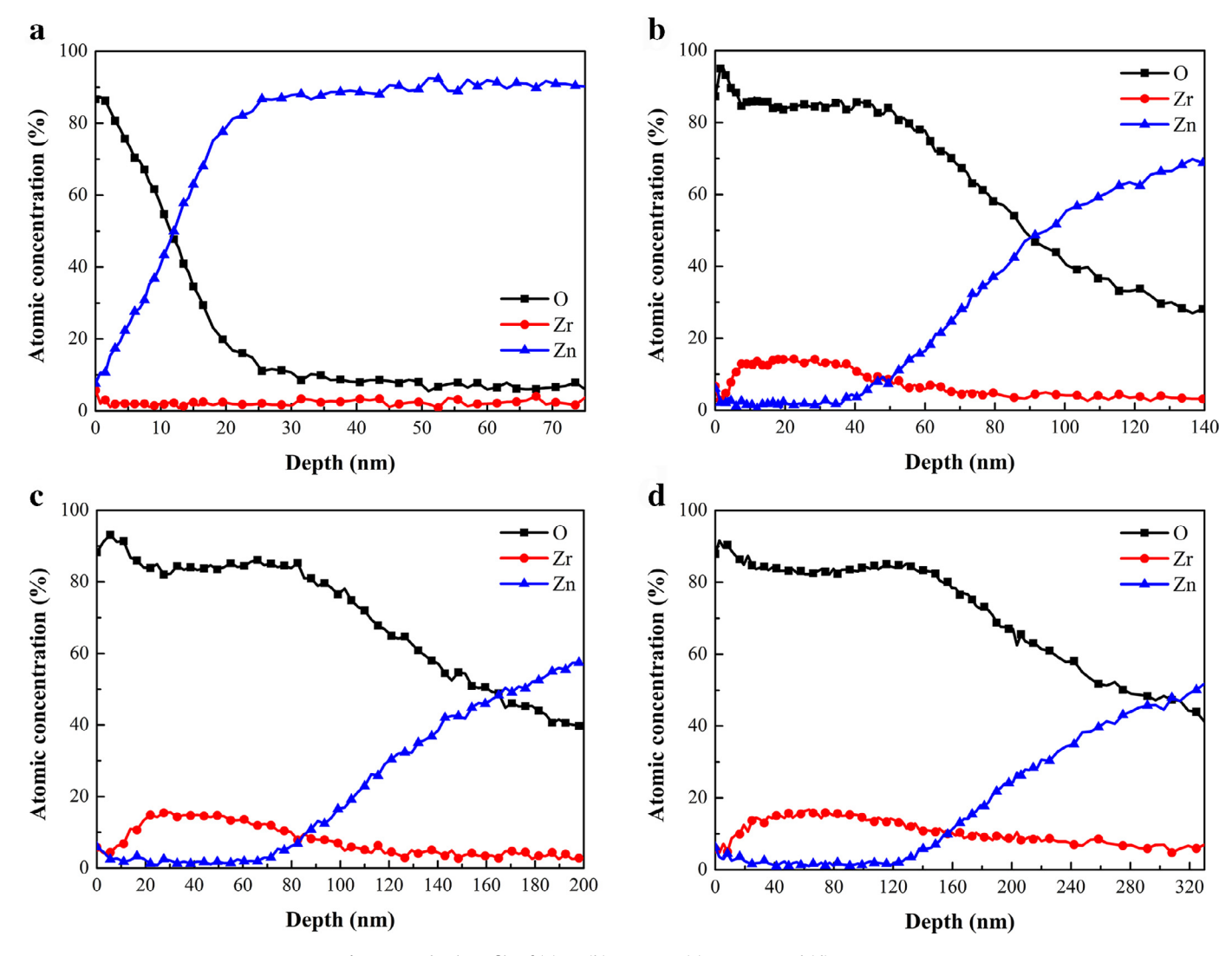


Fig. 3. AES depth profile of (a) ZL, (b) ZrO<sub>2</sub>-100, (c) ZrO<sub>2</sub>-300 and (d) ZrO<sub>2</sub>-500.

Zr 3d (Fig. 2d) and O 1s (Fig. 2e) confirmed the successful deposition of ZrO<sub>2</sub>. In addition, as shown in Fig. 2c, the peak intensity of Zr 3d enhanced with increased deposition cycles. The Zr 3d core-level peaks was deconvoluted, showing doublets of Zr  $3d_{5/2}$  (182.3 eV) and Zr  $3d_{3/2}$  (184.7 eV) with a constant spin-orbit splitting of 2.4 eV. In addition, the intensity ratio of Zr  $3d_{5/2}$  and Zr  $3d_{3/2}$  peaks was approximately 3:2, consistent with the theoretical value for Zr<sup>4+</sup> [30]. These suggested that ZrO<sub>2</sub> phases were generated [31,32]. The slight shift of Zr 3d peak was ascribed to the formation of amorphous zirconia or hydrous zirconia [33,34]. The high resolution of O 1s spectra can be fitted into two peaks: O<sup>2-</sup> for the ZrO<sub>2</sub> (530.1 eV) and –OH group for the Zr-OH (531.9 eV) [35-37].

Furthermore, the depth profile of element composition of Zn-0.1Li alloy samples before and after ZrO<sub>2</sub> deposition are displayed in Fig. 3. The Zr depth profile presented a gradient change along with the depth direction after ALD treatment. Such gradual transition of coating composition could overcome potential mismatch in mechanical properties between the coating and substrate. The deposited layer was mainly composed of Zr and O, with undetectable Zn. It indicated that element Zr existed in the form of its oxide, consistent with the XPS spectra in Fig. 2. The maximum atomic concentrations of Zr were approximately 14%, 16% and 17% for ZrO<sub>2</sub>-100, ZrO<sub>2</sub>-300 and ZrO<sub>2</sub>-500 samples, respectively

(Fig. 3b-d). With successive depositions, the film thickness increased from ~40 nm (for 100 cycles) to ~120 nm (for 500 cycles).

## 3.2. Electrochemical evaluation

Fig. 4 shows the results of short-term electrochemical corrosion tests, including potentiodynamic polarization curves and Nyquist plots. Corresponding electrochemical parameters were calculated (Fig. 4d-e). It could be seen that the corrosion current density decreased gradually with increasing ALD deposition cycles. The corrosion rates were ranked in a descending order: ZL> ZrO<sub>2</sub>- $100 > ZrO_2-300 > ZrO_2-500$ . The corrosion rate of  $ZrO_2-500$  $(0.054 \pm 0.014 \text{ mm/year})$  was almost 5 times smaller than that of ZL (0.286  $\pm$  0.012 mm/year), indicating outstanding corrosion resistance of the ZrO2 layer. The electrochemical impedance spectroscopies (EIS) of ZL and ZrO2-100 were characterized by two capacitive loops and one inductive loop (Fig. 4b). The presence of inductive loop was associated with the formation, adsorption and desorption of corrosion products, indicating the dissolution of metal substrate. With further increased deposition cycle, the inductive loop was absent in ZrO2-300 and ZrO2-500, along with an apparently enlarged capacitive arc. The diameter of a capacitive loop was directly correlated to the corrosion resistance. In addition, the values of the impedance modulus, |Z| at the lowest

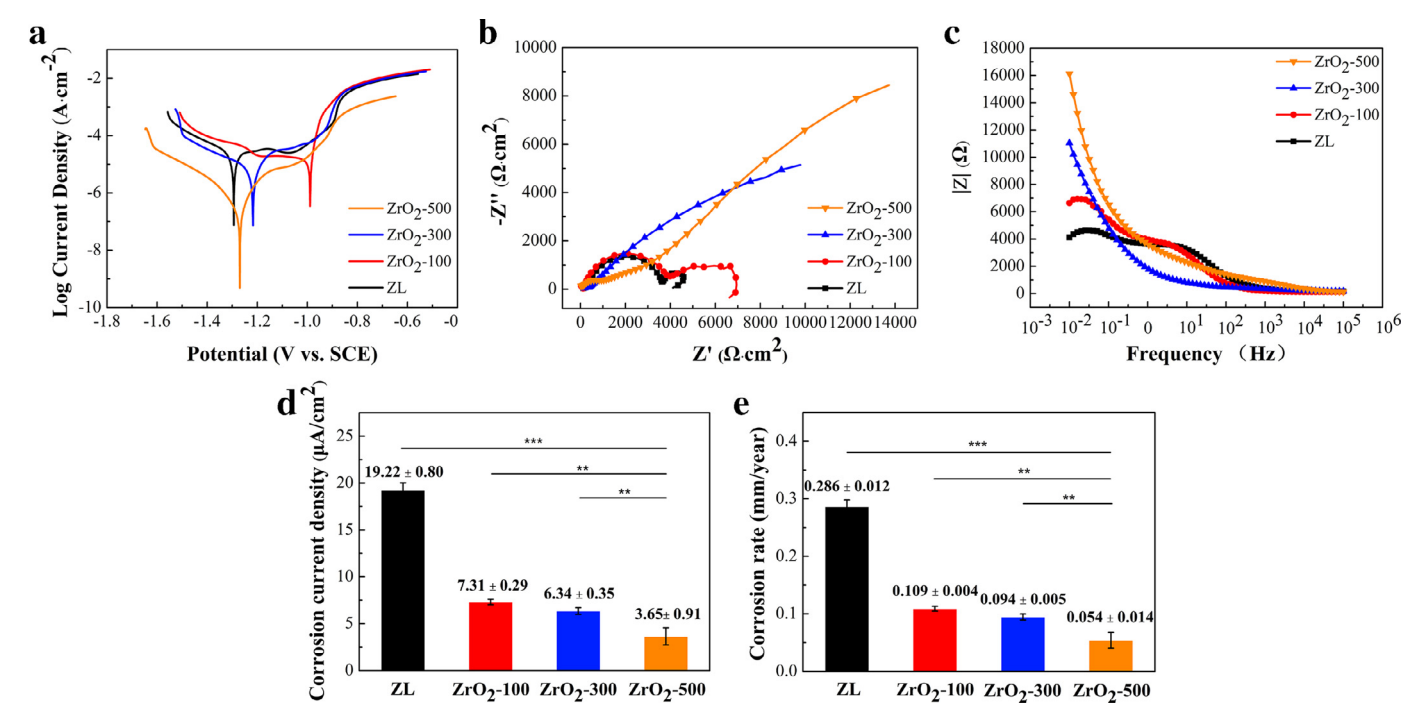


**Fig. 4.** Electrochemical measurements of ZL,  $ZrO_2$ -100,  $ZrO_2$ -300 and  $ZrO_2$ -500 in Hanks' solution: (a) Potentioldynamic curves; (b) Nyquist plots; (c) Bode plots of |Z| vs. frequency. Electrochemical parameters calculated by Tafel region extrapolation: (d) corrosion current density and (e) corrosion rate. (\*P < 0.05, \*\*P < 0.01, and \*\*\*P < 0.001).

frequency, were consistent with the results of capacitive loops (Fig. 4c). Hence, it can be concluded that ALD of ZrO<sub>2</sub> remarkably enhanced the corrosion resistance of Zn-0.1Li alloy.

## 3.3. Immersion tests

The long-term degradation behavior of Zn-0.1Li alloy with and without ALD treatment was investigated by immersion test in Hanks' solution at 37 °C for 28 days (Fig. 5). The surface morphologies of samples are displayed in Fig. 5a. Serious corrosion created plenty of corrosion pits on the uncoated ZL alloy (Fig. 5a1). Instead, only a few cracks were presented after ZrO2 deposition (Fig. 5a2a4). Additionally, samples fabricated under the condition of more deposition cycles had fewer and less severe cracks. XRD, XPS and EDS mapping were used to further investigate the composition of corrosion products (Fig. 5b-e). For both ZL and ZrO<sub>2</sub>-500, Zn, O and P were the major elements of their corrosion products (Fig. 5b-c). XRD detected Zn<sub>3</sub>(PO<sub>4</sub>)<sub>2</sub>·4H<sub>2</sub>O as the primary crystalline product (Fig. 5d). In addition, no residual Zr was observed after 28 days' immersion according to the XPS analysis (Fig. 5e). The change of pH value was in consistent with the corrosion tendencies (Fig. 5f). The first 3 days witnessed the most rapid increase in pH values, followed by a near-plateau state in both bare and ZrO2-coated group. In addition, the release of Zn<sup>2+</sup> in Hanks' solution was significantly reduced by the ALD treatment, from 49.55  $\pm$  4.94  $\mu g/ml$ for ZL to 7.21  $\pm$  3.33  $\mu g/ml$  for ZrO<sub>2</sub>-500  $\mu g/ml$  in the end of immersion. However, an opposite trend was observed in terms of Li+ release (Fig. 5g).

### 3.4. In vitro cytocompatibility

We further examined the effects of material extracts of bare and  $ZrO_2$ -deposited Zn-0.1Li alloy samples on cell viability, as displayed in Fig. 6a. The viability of MC3T3-E1 cells cultured in the extract of ZL alloy was  $9.80\% \pm 3.03\%$ , and it decreased further in the following incubation. In stark contrast, the samples

with  $ZrO_2$  deposition elicited much higher viabilities and thus improved cytocompatibility, with the  $ZrO_2$ -500 ranked as the best. The ion concentrations in the extracts were analyzed and are shown in Fig. 6b. Interestingly,  $ZrO_2$  deposition decreased the  $Zn^{2+}$  concentration but increased the  $Li^+$  ion concentration. In addition, there is no obvious difference between the pH values of the extracts of ZL and  $ZrO_2$ -coated samples as shown in Fig. 6c.

Moreover, the effects of ZrO<sub>2</sub> coating on cell behavior were evaluated via laser scanning confocal microscopy (LSCM) in terms of cell attachment, spreading and cytoskeleton organization, as shown in Fig. 6d. Initially, the majority of adherent cells on all substrates except for ZrO<sub>2</sub>-500 presented a round shape, although the cell spreading was slightly better in the ZrO<sub>2</sub>-300 group in contrast to the ZL and ZrO<sub>2</sub>-100 groups. Differently, osteoblasts were able to adhere to and spread well on ZrO<sub>2</sub>-500, exhibiting a multi-polar spindle morphology with a number of cytoplasmic extensions and filopodia, as well as a contiguous and healthy cytoskeleton structure.

## 3.5. In vivo tests

## 3.5.1. Degradation behavior

In order to investigate the changes in structure and composition of degradation layer, the cross-sections of bone-implant interface were investigated via backscattered electron (BSE) images and EDS images, as shown in Fig. 7. After implantation for 4 weeks, the surface of ZL was covered by a layer of degradation product, which was mainly composed of Zn, O, Ca and P. However, only limited surface of ZrO<sub>2</sub>-500 was occupied by degradation products with similar composition, indicating a delayed corrosion behavior after ALD treatment. At week 8, the surrounding area of ZrO<sub>2</sub>-500 implant was completely occupied by newborn bone (Fig. 7b). In addition, the degradation products were in close contact with the bone tissue. In contrast, fewer discontinuous bone tissues were found newly formed around ZL. After 12 weeks of implantation,

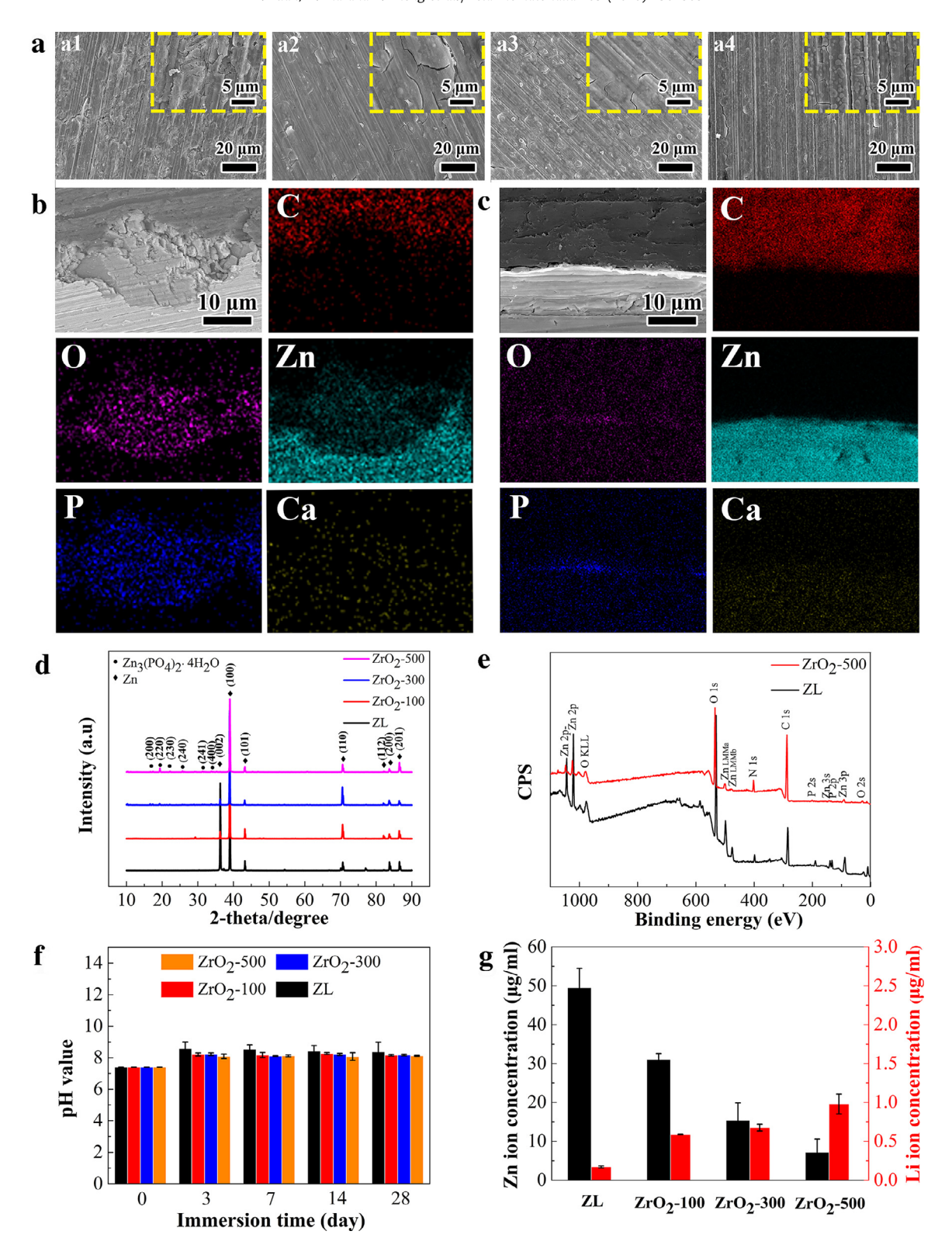


**Fig. 5.** In vitro immersion assay for 28 days in Hanks' solution. (a) Surface morphologies of samples with and without ALD treatment: (a1) ZL, (a2) ZrO<sub>2</sub>-100, (a3) ZrO<sub>2</sub>-300, and (a4) ZrO<sub>2</sub>-500. EDS mapping of corrosion products of (b) ZL and (c) ZrO<sub>2</sub>-500. (d) XRD pattern of the corrosion products. (e) XPS analysis of corrosion products on ZL and ZrO<sub>2</sub>-500. (f) pH evolution over immersion time. (g) Zn and Li ion concentrations at the end of immersion.

the degradation products were diffused towards the surrounding tissue in both ZL and  $\rm ZrO_2$ -500 group. Meanwhile, thicker and denser newborn bone was found in the surrounding of  $\rm ZrO_2$ -500 while the newborn bone around ZL still remained incomplete and unsubstantial (Fig. 7c).

# 3.5.2. Histological analysis

Often, the degradation products of implantable biomaterials have significant effects on their tissue environment. Here, the response of bone tissue towards ZL and  $\rm ZrO_2$ -500 implant was investigated via histological staining of the implant-tissue using

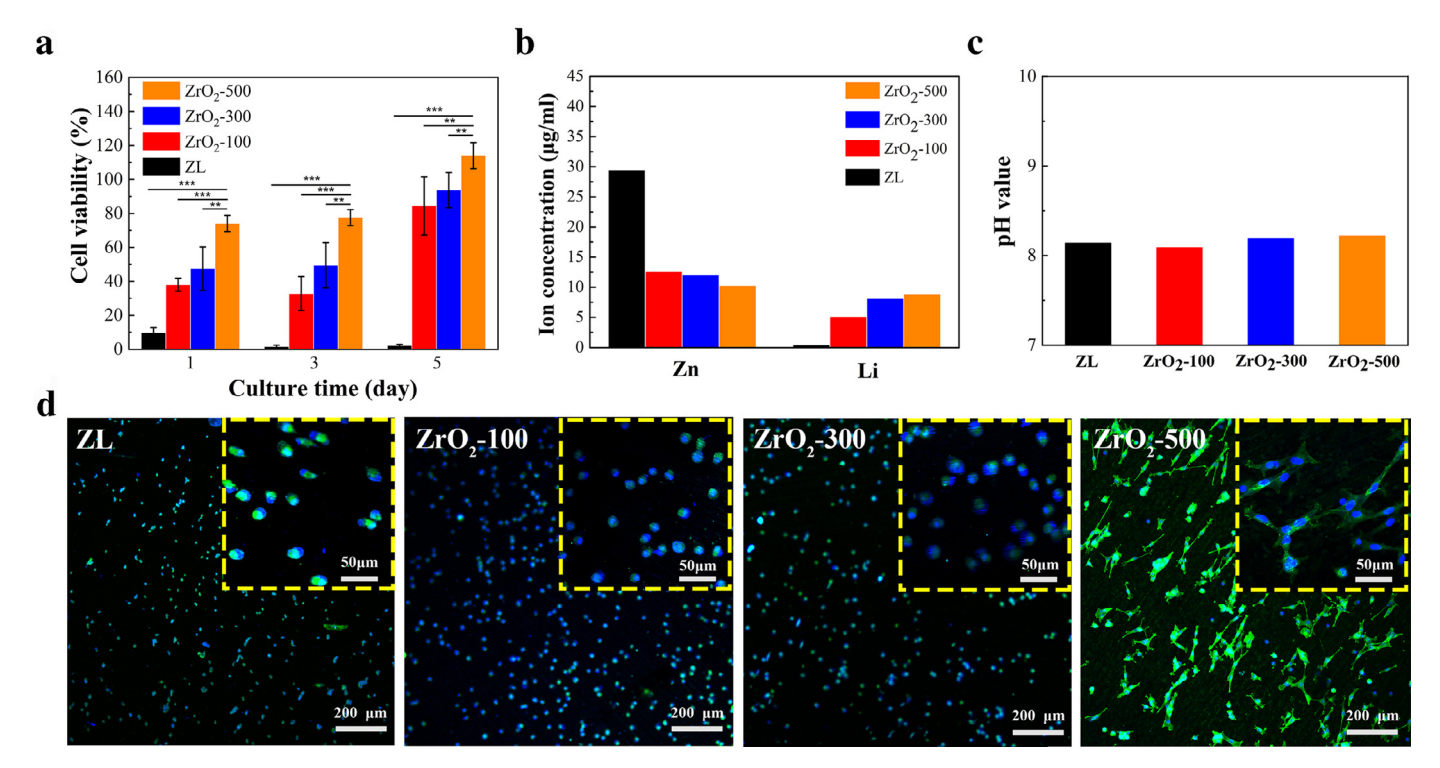


**Fig. 6.** (a) Viability of MC3T3-E1 cells cultured in the extracts of bare and  $ZrO_2$ -coated samples. (b) Ion concentrations of culture media incubated with the samples for 24 h. (c) pH values of the sample extracts. (d) LSCM images of MC3T3-E1 cells cultured on bare and  $ZrO_2$ -treated samples. The actin cytoskeleton (green) and the nucleus (blue) were counterstained. (\*P < 0.05, \*\*P < 0.01, and \*\*\*P < 0.001). (For interpretation of the references to colour in this figure legend, the reader is referred to the web version of this article.)

methylene blue and basic fuchsin sections, as shown in Fig. 8. After 8 weeks postoperatively, limited woven bone was formed around the ZL implants. On the contrary, the peri-implant area in ZrO<sub>2</sub>-500 group was almost filled by newly formed bone, indicating a beneficial effect of ALD treatment on new bone formation. Meanwhile, a layer of fibrous connective tissue was presented between the bone tissue and implant in both groups at week 8, resulting in weak osseointegrantion. As the implantation prolonged to 12 weeks, much more new bone was deposited in the peri-implant area for both groups. Specifically, local peripheral pitch of the ZrO<sub>2</sub>-500 was in close contact with the surrounding bone tissue, signifying a certain degree of osseointegrantion. However, the fibrotic layer remained around ZL, separating the newly formed bone from bonding the implant.

To further investigate the inflammatory response, the decalcified samples were stained by hematoxylin and eosin (H&E) (Fig. 9). After 8 weeks postoperatively, the local inflammatory infiltration of macrophages and lymphocytes was observed in the ZL group. Meanwhile, a loose osteoid tissue was presented surrounding the implant. In contrast, few inflammatory cells were presented in the ZrO<sub>2</sub>-500 group, indicating a beneficial effect of ALD treatment on the inflammatory response. Pleasingly, the implant was surrounded by a relatively dense osteoid tissue. The mature degree of newly bone was also assessed by Masson's trichrome (MT) staining. The mature bone tissue was stained blue, while the immature bone tissue red. In the ZrO<sub>2</sub>-500 group, the new bone integrated well with the host bone. Besides, the peri-implant bone tissue mainly consisted of mature bone. On the contrary, there was much more immature bone in the surrounding of implant in ZL group. At week 12, fibrous tissue encapsulation was observed in both groups. Inflammatory reaction was still detected along with unordered fibroblast growth in the ZL group. By comparison, an ordered cell growth was found in the ZrO<sub>2</sub>-500 group with minimal inflammatory response. The thickness of bone tissue surrounding the implant also increased with more compact structure.

Furthermore, histological response of organic tissue was investigated to evaluate the comprehensive toxicity of degradation products during their metabolism and excretion process (Fig. 10). The histological evaluation displayed that no significant pathological changes (tissue damage, inflammation and lesions, etc.) took place in heart, liver, spleen lung and kidney after 8- and 12-week's implantation. The local responses of peri-implant tissue to the releasing degradation products affect bone tissue healing and denote the biosafety of the implant materials. The histological results after 12 weeks' implantation demonstrated that both groups were biosafe, causing minimal functional disorder or lesions.

# 4. Discussion

# 4.1. Feasibility of ZrO<sub>2</sub> coating on BMs via ALD treatment

On account of its favorable combination of physiochemical and mechanical properties, ZrO<sub>2</sub> has been wildly applied in bone repair and replacement. ZrO<sub>2</sub> can stimulate the adhesion, proliferation and differentiation of osteoblast cells [38,39]. *In vivo* studies also confirmed direct bone apposition and favorable osseointegration of ZrO<sub>2</sub> implants [40]. The successful application of ZrO<sub>2</sub> implants suggests the potential of ZrO<sub>2</sub> as a coating material. ZrO<sub>2</sub> coating has been applied on the surface of 316 stainless steel [41] and titanium [42] for the sake of antibacterial property and corrosion resistance. In addition, ZrO<sub>2</sub> was employed on the surface of Mg-based alloys to promote corrosion resistance and biocompatibility as well [15,43]. However, when it comes to biodegradable metals, there are controversies in the application of ZrO<sub>2</sub> coatings since they are generally bio-inert and non-degradable in physiological environment.

There have thus far been few literature reports on the *in vivo* metabolism of ZrO<sub>2</sub> coating in orthopedic environment. Nevertheless, the bio-distribution of ZrO<sub>2</sub> wear debris generated in total hip or knee replacement had been documented. The release of ZrO<sub>2</sub>

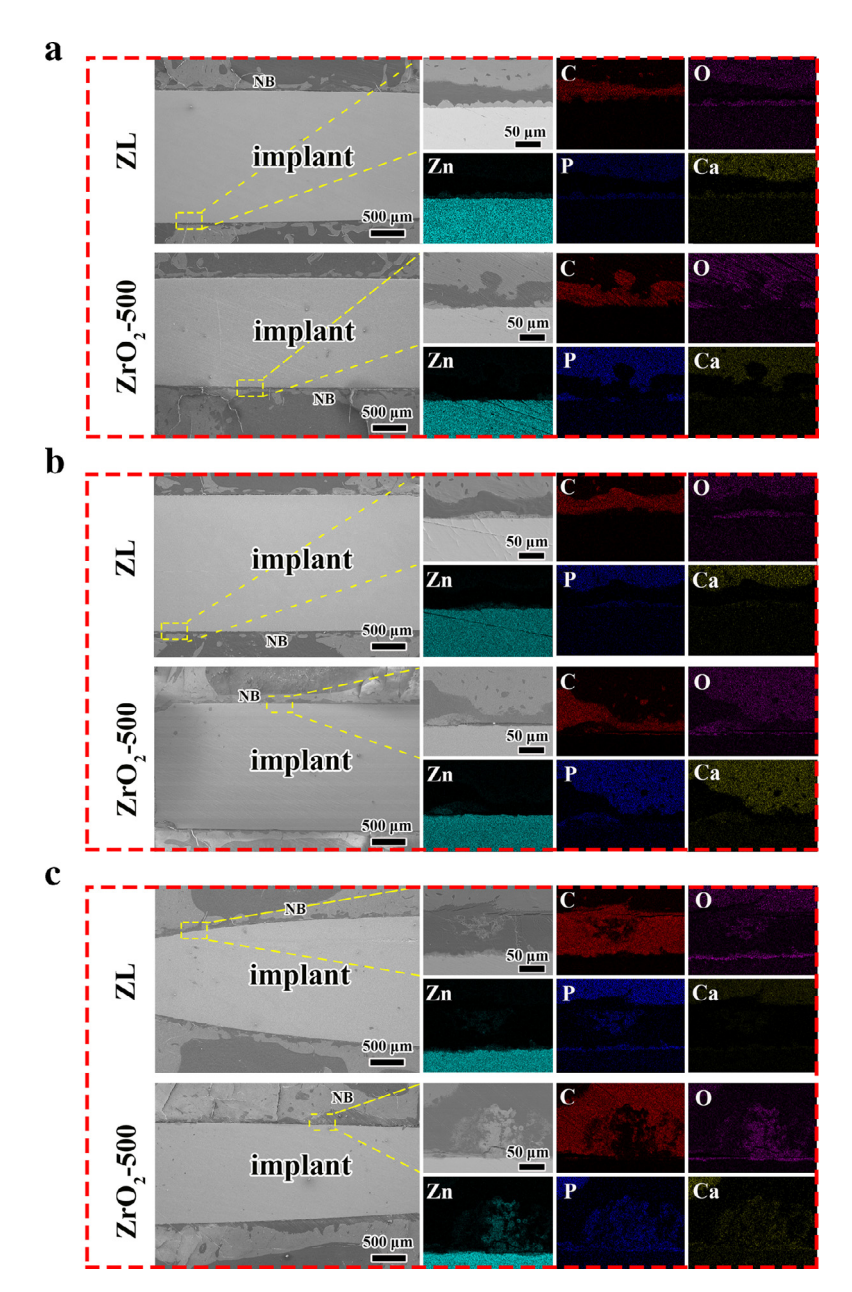


Fig. 7. SEM images of the cross-sections of ZL and ZrO<sub>2</sub>-500 for (a) 4 weeks, (b) 8 weeks and (c) 12 weeks. NB: new bone. In addition, the right panels show corresponding EDS maps of elements of interest for the rectangular areas in (a-c).

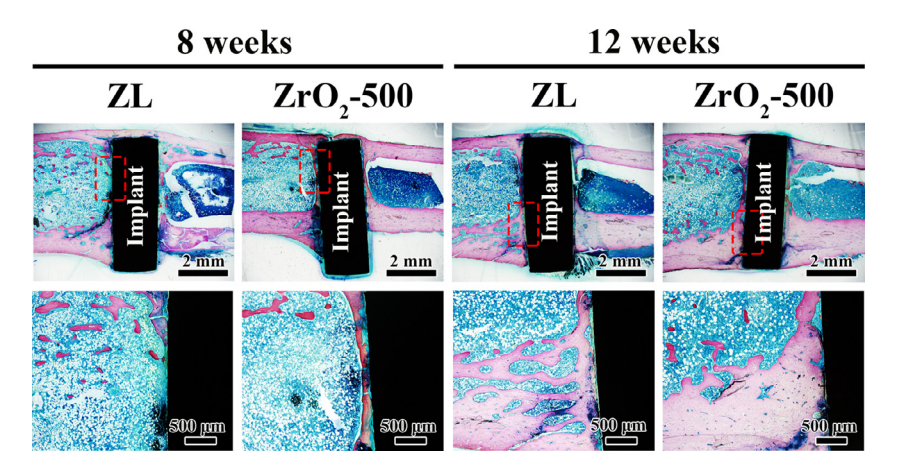


Fig. 8. Hard tissue sections of the bone-implant interfaces after various implantation periods. The red rectangles are zoomed in for clarity. (For interpretation of the references to colour in this figure legend, the reader is referred to the web version of this article.)

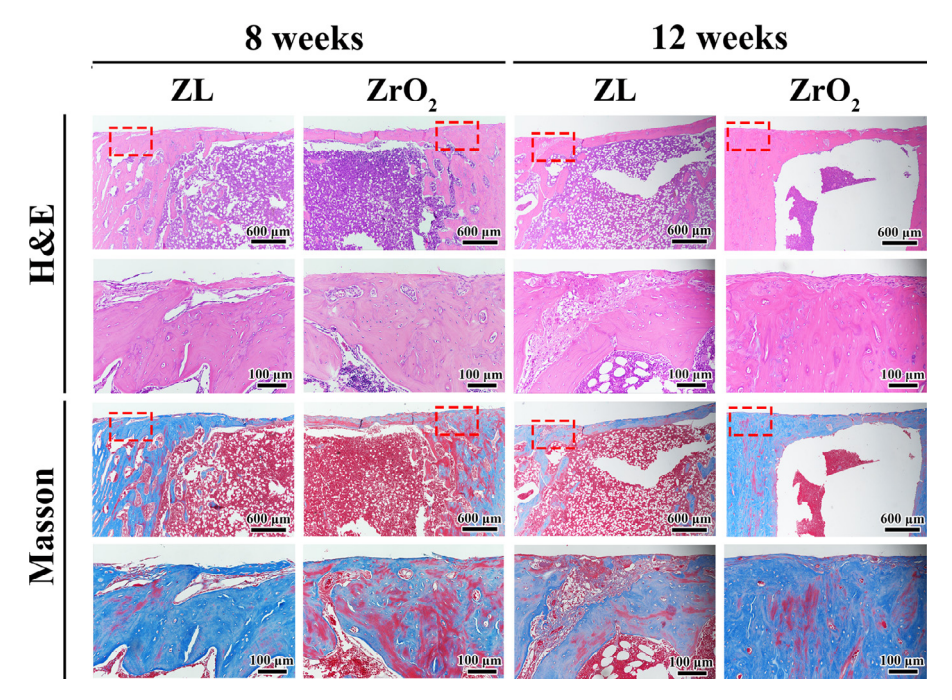


Fig. 9. Histological analysis of decalcified samples. H&E and Masson's trichrome staining of ZL and ZrO<sub>2</sub>-500 after 8- and 12-week implantation (The red rectangles are magnified). (For interpretation of the references to colour in this figure legend, the reader is referred to the web version of this article.)

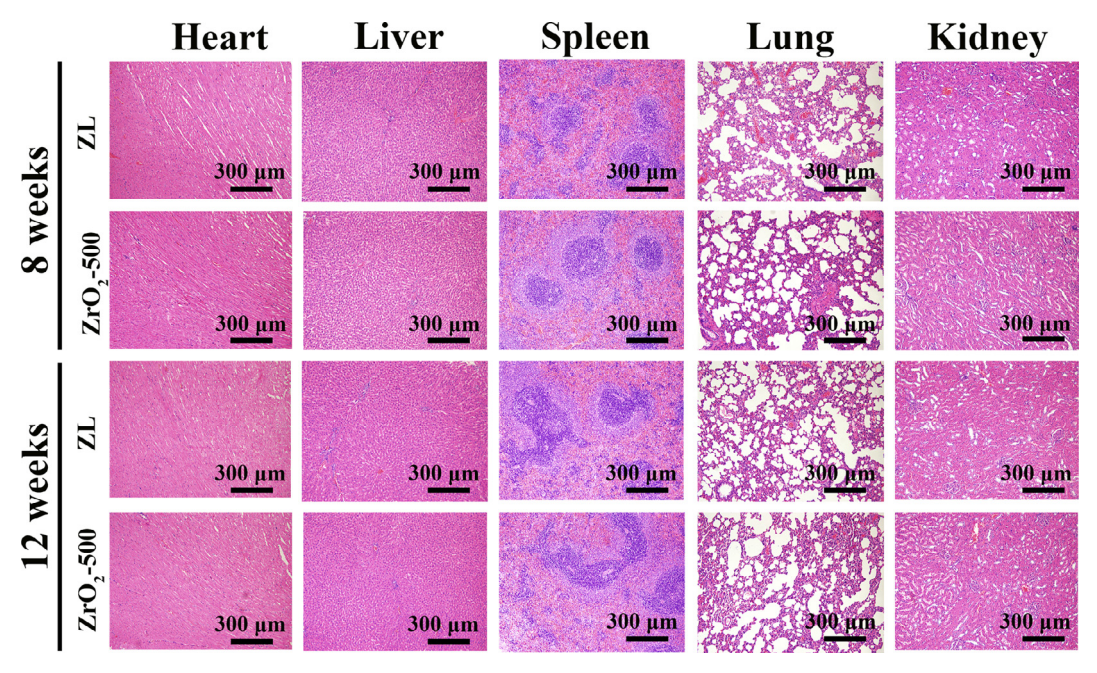


Fig. 10. Histological images of diverse organs after 8 and 12 weeks of implantation of ZL and ZrO<sub>2</sub>-500.

particles might raise local and systematic biosafety issues. Wear particles are mainly transported by means of lymphatic system [44]. When the size of wear particle is smaller than 10 μm, they can be phagocytized or pinocytosed by macrophages and foreign body giant cells. Subsequently, they enter the lymphatic system [45]. Meanwhile, a debris particle is able to activate macrophages, which then release inflammatory mediators and trigger osteoclastic bone resorption, resulting in osteolysis surrounding the implant [46,47]. In addition, the existence of wear particles in the fixed macrophages or Kupffer cells lining the hepatic sinusoids also implied the hematogeous dissemination of the wear particle [44]. Intravenous administration of ZrO<sub>2</sub> nanoparticles in rats demonstrated a major accumulation of ZrO<sub>2</sub> nanoparticles in

spleen, lung and feces [48]. Nonetheless, it is reported that the effects of particle accumulation in organs are dose-dependent in clinical implantation. Adverse impact was found in the case of high concentration, while low concentration displayed no obvious alternation compared with normal tissue [44].

In this work, a better bone formation and osseointegration was achieved instead of bone resorption in the  $\rm ZrO_2$ -500 group. Besides, there was no accumulation of  $\rm ZrO_2$  in all the organs investigated. It is hypothesized that the distinct behaviors between  $\rm ZrO_2$ -based ALD coating and wear debris is attributed to the content of  $\rm ZrO_2$  particles. The wear debris will be persistently released during the enlistment of implants, resulting in aseptic loosening and osteolysis. However, the  $\rm ZrO_2$  coating fabricated by ALD had

a nanoscale thickness. In this way, only limited number of  $\rm ZrO_2$  particles could be generated. Additionally, although  $\rm ZrO_2$  is non-degradable *in vivo*, it is able to be excreted via feces as mentioned above, alleviating the negative effect of accumulation. Therefore,  $\rm ZrO_2$  coating fabricated by ALD is supposed to be a promising alternative to control the corrosion rate of biodegradable metals and improve their biocompatibility.

## 4.2. Biodegradation behavior of Zn-0.1Li alloy after ALD treatment

In physiological milieus, Zn-based BMs majorly degrade through anodic oxidation of Zn into Zn2+ and the cathodic reduction of oxygen Eq. (1) and (2) [49]. The increase in local pH and Zn<sup>2+</sup>can lead to the formation of ZnO and Zn(OH)2 Eq. (3) and (4), establishing a barrier layer on the surface. It is demonstrated that ZnO is more thermodynamically stable in physiological environment compared with Zn(OH)<sub>2</sub> and it makes up the majority of the corrosion products [50]. However, the abundant chloride ions in physiological media will convert ZnO and Zn(OH)<sub>2</sub> into soluble salts, resulting in the breakdown of the protection layer [51]. The subsequent formation of hydrated zinc phosphate is preferred thermodynamically in physiological environment (Eq. (5)) [52], which was confirmed on ZL with and without ALD treatment by EDS and XRD spectra after 28 days' immersion (Fig. 5). Meanwhile, the in vivo results also demonstrated that the corrosion products were mainly composed of Zn, O, Ca and P.

$$Zn \rightarrow Zn^{2+} + 2e^{-} \tag{1}$$

$$2H_2O + O_2 + 4e^- \to 4OH^- \tag{2}$$

$$Zn^{2+} + 2OH^- \rightleftharpoons Zn(OH)_2 \tag{3}$$

$$Zn(OH)_2 \rightarrow ZnO + H_2O \tag{4}$$

$$3Zn^{2+} + 2HPO_4^{2-} + 2OH^- + 2H_2O \rightarrow Zn_3(PO_4)_2 \cdot 4H_2O$$
 (5

ALD has been utilized to deposit barrier layer with well-defined thickness, pinhole-free structure, and good layer conformity [53]. In this research, nanoscale ZrO2 films were deposited on the ZL surface by cyclic reaction between TDMAZ and water. The two self-terminating reactions in the formation process of the ZrO<sub>2</sub> film are illustrated in the Fig. 11. The thickness of ZrO2 coating and ZnO layer increased with the deposition prolonging. In addition to that, the coating structure became more compact with fewer gaps. After ALD treatment, both in vitro and in vivo results demonstrated that the corrosion resistance of ZL was significantly improved. The introduction of the ZrO<sub>2</sub> barrier layer alleviated the direct contact between corrosion media and substrate. As shown in Fig. 3, the proportion of Zn in the surface was reduced after ZrO<sub>2</sub> deposition. The reduction in the reactive Zn is able to slow down the degradation rate. In addition, corrosion-resistant metal oxide will also benefit the corrosion resistance. The introduction of oxygen source can react with Zn on the surface and give rise to a thicker layer of zinc oxide (Fig. 3). It is claimed that ZnO is more persistent than Zn in 0.1 M sodium chloride solution under the circumstance of neutral and alkaline environment [54]. Therefore, the thicker oxide layer will also play a significant role in corrosion resistance. The primary corrosion process of bare and ZrO<sub>2</sub>-coated ZL are illustrated in Fig. 12a and b. In contrast to the direct collision between the corrosion media and substrate in ZL group, the presence of ZrO<sub>2</sub> barrier layer can prevent the substrate from corrosive attacks at the initial stage. With corrosion proceeding, the corrosion media would gradually permeate through the nanogaps in the  $ZrO_2$  layer and react with the substrate. Finally, the  $ZrO_2$  layer would be damaged and fail to provide efficient protection (Fig. 5). In this way, the degradation rate of ZL is controllable via deposition thickness of  $ZrO_2$ . Meanwhile, the inner thicker ZnO layer is also able to provide superior corrosion resistance in contrast to ZL group. However, as mentioned above, ZnO is not stable in physiological environment, and therefore will gradually dissolve and be substituted by the formation of hydrated zinc phosphate of better stability (Figs. 5 and 7).

The degradation of Li-rich phase consists of two types of corrosion models, thus chemical dissolution and electrochemical corrosion were investigated in this research. The former, as involved in the gradual dissolution in the physiological condition, can be observed in both ZrO2-coated and bare samples. The later includes the formation of micro-galvanic coupling among coating, matrix and Li-rich phase (Fig. 12b1-b2). In consideration of the differences in standard electrode potential, Li is prone to be attacked with a lower standard electrode potential when the corrosion media penetrated through the nanogaps of ZrO2 layer while Zn matrix was protected in physiological condition (Fig. 12b1) [55]. Besides, it is reported that galvanic coupling can form between Zn and ZnO, accelerating the corrosion rate of Zn [56-58]. In this way, the accelerated release of Li+ after ZrO2 deposition may be attributed to the formation of galvanic coupling between ZnO layer and Li-rich phase in the matrix (Fig. 12b2). The increment in ZnO species on the surface with increased deposition cycles might have resulted in the formation of more micro-galvanic coupling between ZnO and Li-rich phase. Previous research has also revealed Mg-rich phases would corrode preferentially compared with Zn matrix in Zn-Mg composite due to a potential gradient [59].

### 4.3. Biocompatibility of Zn-0.1Li alloy after ALD treatment

A biphasic effect of Zn ion on the cell behavior was observed depending on the Zn ion concentration. Low dose of Zn<sup>2+</sup> is able to stimulate the bone formation by increasing osteoblast proliferation, mineralization osteoblast marker gene expressions as well as calcium deposition [60–62]. In our previous research, Zn<sup>2+</sup> was found to stimulate the growth and apoptosis of osteoblast-like cell simultaneously while the process of cell apoptosis was dominant at high Zn<sup>2+</sup> concentrations [7]. In addition, high-dose Zn<sup>2+</sup> could interfere the electron transport in uncoupled mitochondria reversibly and result in cell injury [63,64]. An excess release of Zn<sup>2+</sup> was shown to cause significant cytotoxicity *in vitro* and delayed osseointegration *in vivo* after the implantation of Zn-based BMs [9,65]. Hence, the systematic and local toxicity of Zn-based alloys remain concerns.

In the present research, significant cytotoxicity of ZL to MC3T3-E1 cell was observed in vitro. After coating with ZrO2, the released Zn<sup>2+</sup> was significantly reduced. As a consequence, improved cell viability and superior cell spreading were observed in ZrO2-coated group since the influence of Zn<sup>2+</sup> on biocompatibility is dosedependent. Meanwhile, the cytocompatiblity was further improved with increased deposition cycles. In vivo results also demonstrated superior new bone formation in the surrounding of ZrO<sub>2</sub>-500 at week 8 compared with ZL. Subsequently, such difference became more obvious at week 12 (Fig. 7). In addition, better osseointegration was achieved with evident direct bonding between the ZrO2-500 implant and new bone at week 12 (Fig. 8). In the early stage of implantation, tissue trauma will lead to more accumulation of body fluids. Meanwhile, a haematoma consisted of cells from peripheral and intramedullary blood and bone marrow is generated, accompanied with acute inflammatory response [66]. Hence, an accelerated corrosion releasing more degradation products can be expected in this period. However, the overdose of Zn<sup>2+</sup> would suppress bone formation and induce side effects. Limited contacts

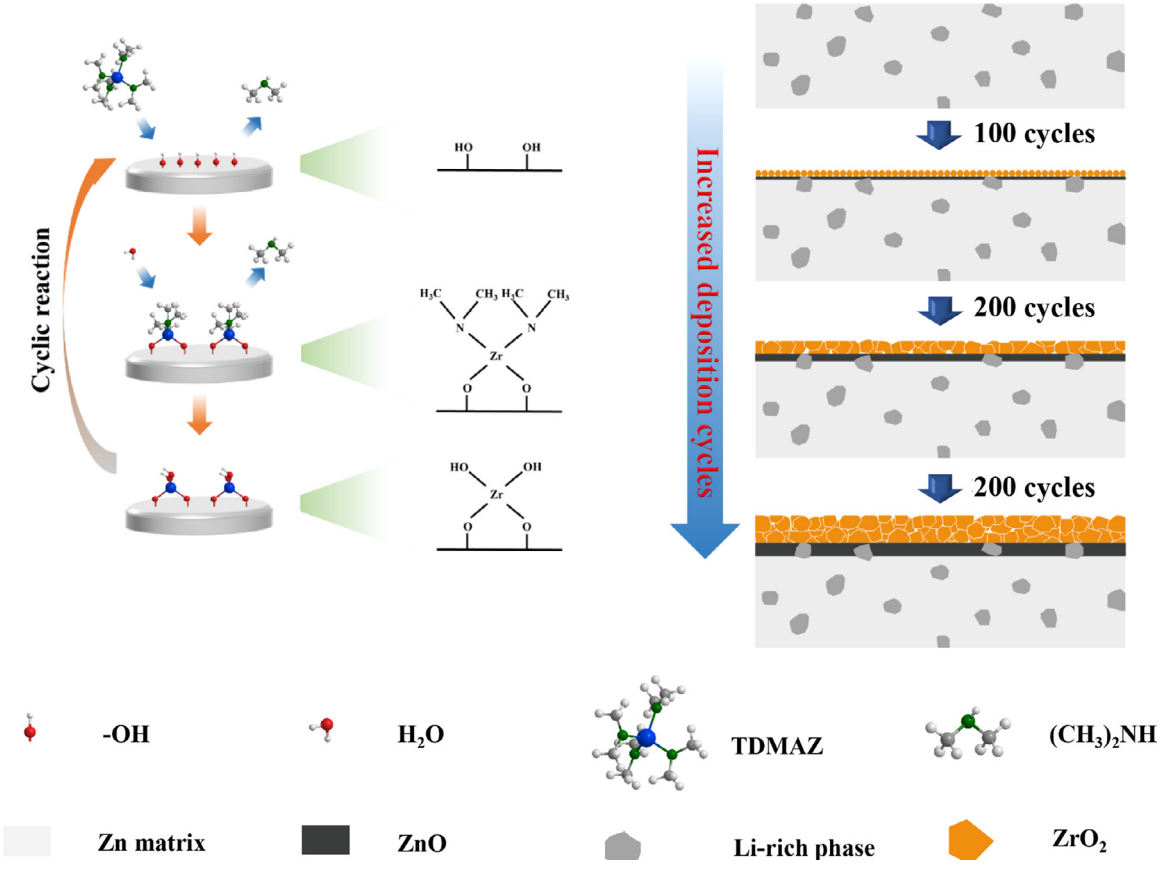


Fig. 11. Schematic illustration of ZrO<sub>2</sub> deposition process via atomic layer deposition.

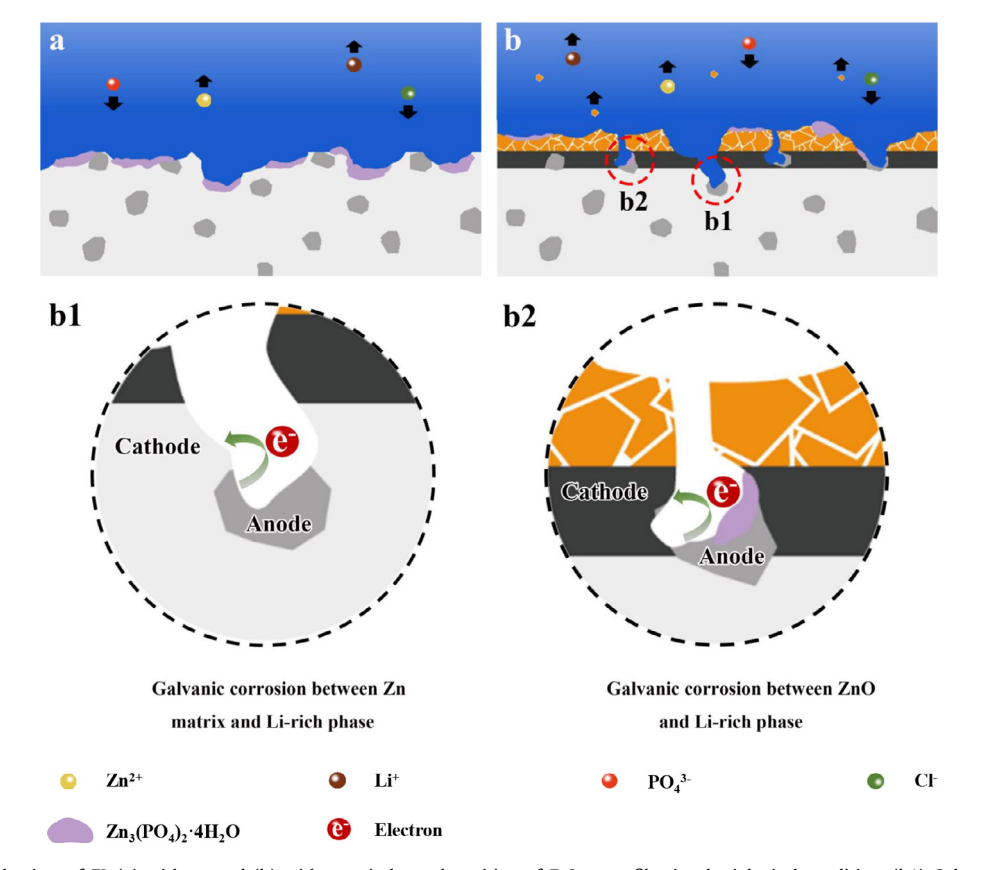


Fig. 12. Degradation mechanism of ZL (a) without and (b) with atomic layer deposition of ZrO<sub>2</sub> nanofilm in physiological condition. (b1) Galvanic corrosion between Zn matrix and Li-rich phase, (b2) galvanic corrosion between ZnO and Li-rich phase.

between bone and implant, significant inflammatory response, as well as massive fibrous connective tissue capsulation were found in the surrounding of pure Zn due to high dose release of Zn<sup>2+</sup>when implanted into the femoral condyles of Sprague–Dawley rats [59]. In vivo results revealed that zinc-containing  $\beta$ -tricalcium phosphate ceramics could improve new bone formation with zinc content of 0.316 wt.%, while the incorporation of 0.633 wt.% of Zn caused apparent bone resorption [67]. In this way, ZrO<sub>2</sub> coating deposited by ALD treatment could effectively isolate the substrate from the body fluid, hence retarding the releasing rate of Zn<sup>2+</sup>. Under the circumstance of low Zn<sup>2+</sup> concentration, the beneficial effect of Zn<sup>2+</sup> on bone formation is therefore dominant.

In addition, ALD treatment also gave rise to higher levels of Li+. The concentration of Li+ was significantly increased from  $0.50 \mu g/ml$  for ZL to  $8.89 \mu g/ml$  for  $ZrO_2$ -500 (Fig. 6). Li has been extensively applied as a mood stabilizer in the treatment of mood disorders for over half a century. Meanwhile, Li-containing biomaterials are to promote the proliferation and differentiation of osteoblasts in vitro as well bone regeneration in vivo [68,69]. It is reported that Li incorporated  $\beta$ -tricalcium phosphate can further stimulate proliferation and differentiation of human bone marrow stromal cells with Li ion concentrations ranging from 0.23  $\pm$  0.01 to 7.42  $\pm$  0.05 µg/ml in material extract [70]. Li-containing mesoporous bioglass also showed beneficial effect on the proliferation and differentiation of bone mesenchymal stem cells with daily release from approximately 8 µg/ml to 17 µg/ ml in cell culture medium through activation of the Wnt signaling pathway [71]. Hence, it is hypothesized that the elevated release of Li<sup>+</sup> after ALD treatment also played an important role in the improvement of biocompatibility.

#### 5. Conclusions

In this work, ZrO<sub>2</sub> nanofilm was constructed on Zn-Li alloys via ALD to control biocorrosion for orthopedic applications. The introduction of ZrO<sub>2</sub> layer as well as thicker ZnO layer after ALD treatment retarded the corrosion of Zn-0.1Li, showing promise as an effective physical barrier. Meanwhile, the corrosion rate can be controlled by adjusting the ALD deposition cycles. The delayed corrosion allowed a stable and biocompatible implant surface for cell attachment and growth, resulting in enhanced cytocompatibility *in vitro*. Moreover, *in vivo* assays demonstrated better bone formation and osseointegration. To sum, this study introduced a simple, effective and controllable approach to improve the corrosion resistance and biocompatibility of Zn-based materials, while providing insights into the potential mechanisms.

## **Declaration of Competing Interest**

The authors declare that they have no known competing financial interests or personal relationships that could have appeared to influence the work reported in this paper.

## Acknowledgements

This work was supported by the National Key R&D Program of China (Grant No. 2018YFE0104200), the State Key Laboratory for Mechanical Behavior of Materials (Grant No. 20182011), the National Natural Science Foundation of China (Grant No. 51931001, 51431002, 51871004, 51901003 and 81970908), the NSFC/RGC Joint Research Scheme (Grant No. 5161101031), and the Peking University Medicine Seed the Key Research and Development Program of Ningxia Hui Autonomous Region (Grant No. 2018BEG02012).

#### References

- [1] Y.F. Zheng, X.N. Gu, F. Witte, Biodegradable metals, Mater. Sci. Eng., R 77 (2014)
- [2] J. Cheng, B. Liu, Y.H. Wu, Y.F. Zheng, Comparative in vitro Study on Pure Metals (Fe, Mn, Mg, Zn and W) as biodegradable metals, J. Mater. Sci. Technol. (Shenyang, China) 29 (7) (2013) 619–627.
- [3] P.J. Aggett, J.T. Harries, Current status of zinc in health and disease states, Arch. Dis. Child 54 (1979) 909–917.
- [4] K.M. Hambidge, N.F. Krebs, Zinc deficiency: a special challenge, J. Nutr. 137 (4) (2007) 1101–1105.
- [5] H.F. Li, X.H. Xie, Y.F. Zheng, Y. Cong, F.Y. Zhou, K.J. Qiu, X. Wang, S.H. Chen, L. Huang, L. Tian, L. Qin, Development of biodegradable Zn-1X binary alloys with nutrient alloying elements Mg, Ca and Sr, Sci. Rep. 5 (2015) 10719.
- [6] N.S. Murni, M.S. Dambatta, S.K. Yeap, G.R. Froemming, H. Hermawan, Cyto-toxicity evaluation of biodegradable Zn-3Mg alloy toward normal human osteoblast cells, Mater. Sci. Eng., C 49 (2015) 560–566.
- [7] W. Yuan, B. Li, D. Chen, D. Zhu, Y. Han, Y. Zheng, Formation mechanism, corrosion behavior, and cytocompatibility of microarc oxidation coating on absorbable high-purity zinc, ACS Biomater, Sci. Eng. 5 (2) (2018) 487–497.
- [8] D. Zhang, C.S. Wong, C. Wen, Y. Li, Cellular responses of osteoblast-like cells to 17 elemental metals, J. Biomed. Mater. Res., Part A 105 (1) (2017) 148–158.
- [9] H. Yang, X. Qu, W. Lin, C. Wang, D. Zhu, K. Dai, Y. Zheng, In vitro and in vivo studies on zinc-hydroxyapatite composites as novel biodegradable metal matrix composite for orthopedic applications, Acta Biomater 71 (2018) 200–214.
- [10] J. Kubásek, D. Vojtěch, E. Jablonská, I. Pospíšilová, J. Lipov, T. Ruml, Structure, mechanical characteristics and in vitro degradation, cytotoxicity, genotoxicity and mutagenicity of novel biodegradable Zn-Mg alloys, Mater. Sci. Eng., C 58 (2016) 24–35.
- [11] P.F. Manicone, P.R. Iommetti, L. Raffaelli, An overview of zirconia ceramics: basic properties and clinical applications, J. Dent. 35 (11) (2007) 819–826.
- [12] A. Yamamoto, R. Honma, M. Sumita, Cytotoxicity evaluation of 43 metal salts using murine fibroblasts and osteoblastic cells, J. Biomed. Mater. Res. 39 (2) (1998) 331–440.
- [13] G. Wang, F. Meng, C. Ding, P.K. Chu, X. Liu, Microstructure, bioactivity and osteoblast behavior of monoclinic zirconia coating with nanostructured surface, Acta Biomater 6 (3) (2010) 990–1000.
- [14] X. Liu, A. Huang, C. Ding, P.K. Chu, Bioactivity and cytocompatibility of zirconia (ZrO2) films fabricated by cathodic arc deposition, Biomaterials 27 (21) (2006) 3904–3911.
- [15] Y. Zhao, M.I. Jamesh, W.K. Li, G. Wu, C. Wang, Y. Zheng, K.W.K. Yeung, P.K. Chu, Enhanced antimicrobial properties, cytocompatibility, and corrosion resistance of plasma-modified biodegradable magnesium alloys, Acta Biomater 10 (1) (2014) 544–556.
- [16] J.H. Sui, W. Cai, Formation of ZrO2 coating on the NiTi alloys for improving their surface properties, Nucl. Instrum. Methods Phys. Res., Sect. B 251 (2) (2006) 402–406.
- [17] Z. Yao, H. Gao, Z. Jiang, F. Wang, Structure and properties of ZrO2 ceramic coatings on AZ91D Mg alloy by plasma electrolytic oxidation, J. Am. Ceram. Soc. 91 (2) (2008) 555–558.
- [18] A. Rapacz-Kmita, A. Ślósarczyk, Z. Paszkiewicz, HAp-ZrO2 composite coatings prepared by plasma spraying for biomedical applications, Ceram. Int. 31 (4) (2005) 567-571.
- [19] S. Nagarajan, M. Mohana, P. Sudhagar, V. Raman, T. Nishimura, S. Kim, Y.S. Kang, N. Rajendran, Nanocomposite coatings on biomedical grade stainless steel for improved corrosion resistance and biocompatibility, ACS Appl. Mater. Interfaces 4 (10) (2012) 5134–5141.
- [20] R.W. Johnson, A. Hultqvist, S.F. Bent, A brief review of atomic layer deposition: from fundamentals to applications, Mater. Today 17 (5) (2014) 236–246.
- [21] D.M. Hausmann, E. Kim, J. Becker, R.G. Gordon, Atomic layer deposition of hafnium and zirconium oxides using metal amide precursors, Chem. Mater. 14 (10) (2002) 4350–4358.
- [22] M. Leskela, M. Ritala, Atomic layer deposition chemistry: recent developments and future challenges, Angew. Chem., Int. Ed. Engl. 42 (45) (2003) 5548–5554.
- [23] C. Marichy, M. Bechelany, N. Pinna, Atomic layer deposition of nanostructured materials for energy and environmental applications, Adv. Mater. 24 (8) (2012) 1017–1032.
- [24] L. Huang, K. Su, Y.F. Zheng, K.W.K. Yeung, X.M. Liu, Construction of TiO2/silane nanofilm on AZ31 magnesium alloy for controlled degradability and enhanced biocompatibility, Rare Met 38 (6) (2019) 588-600.
- [25] J. Venezuela, M.S. Dargusch, The influence of alloying and fabrication techniques on the mechanical properties, biodegradability and biocompatibility of zinc: A comprehensive review, Acta Biomater 87 (2019) 1–40.
- [26] S. Zhao, J.-M. Seitz, R. Eifler, H.J. Maier, R.J. Guillory II, E.J. Earley, A. Drelich, J. Goldman, J.W. Drelich, Zn-Li alloy after extrusion and drawing: Structural, mechanical characterization, and biodegradation in abdominal aorta of rat, Mater. Sci. Eng. C 76 (2017) 301–312.
- [27] Y. Dai, Y. Zhang, H. Liu, H. Fang, D. Li, X. Xu, Y. Yan, L. Chen, Y. Lu, K. Yu, Mechanical strengthening mechanism of Zn-Li alloy and its mini tube as potential absorbable stent material, Mater. Lett. 235 (2019) 220–223.
- [28] Q. Yang, W. Yuan, X. Liu, Y. Zheng, Z. Cui, X. Yang, H. Pan, S. Wu, Atomic layer deposited ZrO2 nanofilm on Mg-Sr alloy for enhanced corrosion resistance and biocompatibility, Acta Biomater 58 (2017) 515–526.
- [29] M.C. Tsai, M.H. Lee, C.L. Kuo, H.C. Lin, M.J. Chen, In situ atomic layer nitridation on the top and down regions of the amorphous and crystalline high- K gate dielectrics, Appl. Surf. Sci. 387 (2016) 274–279.

- [30] Z. Tan, S. Li, F. Wang, D. Qian, J. Lin, J. Hou, Y. Li, High performance polymer solar cells with as-prepared zirconium acetylacetonate film as cathode buffer layer. Sci. Rep. 4 (1) (2014).
- [31] Y. Han, Y. Yan, C. Lu, Y. Zhang, K. Xu, Bioactivity and osteoblast response of the micro-arc oxidized zirconia films, J. Biomed. Mater. Res., Part A 88 (1) (2009) 117–127.
- [32] G. Pezzotti, B.S. Bal, M. Zanocco, E. Marin, N. Sugano, B.J. McEntire, W. Zhu, Reconciling in vivo and in vitro kinetics of the polymorphic transformation in zirconia-toughened alumina for hip joints: III. Molecular scale mechanisms, Mater. Sci. Eng., C 71 (2017) 552–557.
- [33] J. He, Y. Li, X. Xue, H. Ru, X. Huang, H. Yang, Separation of fluorine/cerium from fluorine-bearing rare earth sulfate solution by selective adsorption using hydrous zirconium oxide, RSC Adv. 6 (49) (2016) 43814–43822.
- [34] C.Y.K. Lung, E. Kukk, T. Hägerth, J.P. Matinlinna, Surface modification of silica-coated zirconia by chemical treatments, Appl. Surf. Sci. 257 (4) (2010) 1228–1235.
- [35] X.H. Zhu, C.X. Yang, X.P. Yan, Metal-organic framework-801 for efficient removal of fluoride from water, Microporous Mesoporous Mater 259 (2018) 163–170.
- [36] J.K. An, J.T. Kim, G. Kang, N.K. Oh, S.H. Hahm, G. Lee, I.S. Park, J.Y. Yun, ZrO2 film prepared by atomic layer deposition using less viscous cocktail CpZr[N(CH3)2]3/C7H8 precursor and ozone, J. Alloys Compd. 701 (2017) 310–315
- [37] T. Murakami, S. Takemoto, N. Nishiyama, M. Aida, Zirconia surface modification by a novel zirconia bonding system and its adhesion mechanism, Dent. Mater. 33 (12) (2017) 1371–1380.
- [38] U. Hempel, T. Hefti, M. Kalbacova, C. Wolf-Brandstetter, P. Dieter, F. Schlottig, Response of osteoblast-like SAOS-2 cells to zirconia ceramics with different surface topographies, Clin. Oral Impl. Res. 21 (2) (2010) 174–181.
- [39] R. Depprich, M. Ommerborn, H. Zipprich, C. Naujoks, J. Handschel, H.P. Wiesmann, N.R. Kubler, U. Meyer, Behavior of osteoblastic cells cultured on titanium and structured zirconia surfaces, Head Face Med 4 (2008) 29.
- [40] A. Scarano, F.D. Carlo, M. Quaranta, A. Piattelli, Bone response to zirconia ceramic implants: an experimental study in rabbits, J, Oral Implantol 29 (1) (2003) 8–12.
- [41] G.S. Kaliaraj, V. Vishwakarma, K. Kirubaharan, T. Dharini, D. Ramachandran, B. Muthaiah, Corrosion and biocompatibility behaviour of zirconia coating by EBPVD for biomedical applications, Surf. Coat. Technol. 334 (2018) 336–343
- [42] V.K. Balla, W. Xue, S. Bose, A. Bandyopadhyay, Laser-assisted Zr/ZrO2 coating on Ti for load-bearing implants, Acta Biomater 5 (7) (2009) 2800–2809.
- [43] J.J. Zhuang, Y.Q. Guo, N. Xiang, Y. Xiong, Q. Hu, R.G. Song, A study on microstructure and corrosion resistance of ZrO2-containing PEO coatings formed on AZ31 Mg alloy in phosphate-based electrolyte, Appl. Surf. Sci. 357 (2015) 1463–1471.
- [44] R.M. Urban, J.J. Jacobs, M.J. Tomlinson, J. Gavrilovic, J. Black, M. Peoc'h, Dissemination of wear particles to the liver, spleen, and abdominal lymph nodes of patients with hip or knee replacement, J. Bone Joint Surg. Am. 82 (4) (2000) 457
- [45] C. Nich, Y. Takakubo, J. Pajarinen, M. Ainola, A. Salem, T. Sillat, A.J. Rao, M. Raska, Y. Tamaki, M. Takagi, Y.T. Konttinen, S.B. Goodman, J. Gallo, Macrophages-Key cells in the response to wear debris from joint replacements, J. Biomed. Mater. Res., Part A 101 (10) (2013) 3033–3045.
- [46] Z. Xing, L.P. Schwab, C.F. Alley, K.A. Hasty, R.A. Smith, Titanium particles that have undergone phagocytosis by macrophages lose the ability to activate other macrophages, J. Biomed. Mater. Res., Part B 85 (1) (2008) 37–41.
- [47] S. Suñer, J.L. Tipper, N. Emami, Biological effects of wear particles generated in total joint replacements: trends and future prospects, Tribol.-Mater., Surf. Interfaces 6 (2) (2013) 39–52.
- [48] T. Sun, G. Liu, L. Ou, X. Feng, A. Chen, R. Lai, L. Shao, Toxicity induced by zirconia oxide nanoparticles on various organs after intravenous administration in rats, J. Biomed. Nanotechnol. 15 (4) (2019) 728–741.
- [49] X. Liu, J. Sun, K. Qiu, Y. Yang, Z. Pu, L. Li, Y. Zheng, Effects of alloying elements (Ca and Sr) on microstructure, mechanical property and in vitro corrosion behavior of biodegradable Zn–1.5Mg alloy, J. Alloys Compd. 664 (2016) 444–452.

- [50] H. Yang, C. Wang, C. Liu, H. Chen, Y. Wu, J. Han, Z. Jia, W. Lin, D. Zhang, W. Li, W. Yuan, H. Guo, H. Li, G. Yang, D. Kong, D. Zhu, K. Takashima, L. Ruan, J. Nie, X. Li, Y. Zheng, Evolution of the degradation mechanism of pure zinc stent in the one-year study of rabbit abdominal aorta model, Biomaterials 145 (2017) 92–105.
- [51] M. Mouanga, P. Berçot, J.Y. Rauch, Comparison of corrosion behaviour of zinc in NaCl and in NaOH solutions. Part I: Corrosion layer characterization, Corros. Sci. 52 (12) (2010) 3984–3992.
- [52] P.K. Bowen, J. Drelich, J. Goldman, Zinc exhibits ideal physiological corrosion behavior for bioabsorbable stents, Adv. Mater. 25 (18) (2013) 2577–2582.
- [53] A.I. Abdulagatov, Y. Yan, J.R. Cooper, Y. Zhang, Z.M. Gibbs, A.S. Cavanagh, R.G. Yang, Y.C. Lee, S.M. George, Al2O3 and TiO2 atomic layer deposition on copper for water corrosion resistance, ACS Appl. Mater. Interfaces 3 (12) (2011) 4593–4601.
- [54] S. Thomas, N. Birbilis, M. Venkatraman, I. Cole, Corrosion of zinc as a function of pH, Corrosion 68 (1) (2012) 015009-1-015009-9.
- [55] Y. Liu, Y. Zheng, X.H. Chen, J.A. Yang, H. Pan, D. Chen, L. Wang, J. Zhang, D. Zhu, S. Wu, K.W.K. Yeung, R.C. Zeng, Y. Han, S. Guan, Fundamental Theory of Biodegradable Metals—Definition, Criteria, and Design, Adv. Funct. Mater. 29 (18) (2019).
- [56] A.M.S.E. Din, J.M.A.E. Kader, A.T. Kuhn, Pitting Corrosion of Zinc in Aqueous Solutions: III. Effect of anode to cathode surface area ratio on pitting corrosion currents, Br. Corros. J. 15 (4) (2013) 208–211.
- [57] S.M. Wilhelm, Galvanic corrosion caused by corrosion products, In Galvanic Corrosion, ASTM International, 1988.
- [58] X.G. Zhang, Corrosion and electrochemistry of zinc, Springer Science & Business Media. 2013.
- [59] H. Yang, X. Qu, W. Lin, D. Chen, D. Zhu, K. Dai, Y. Zheng, Enhanced osseointe-gration of Zn-Mg composites by tuning the release of Zn ions with sacrificial Mg-rich anode design, ACS Biomater. Sci. Eng. 5 (2) (2018) 453–467.
- [60] G. Jin, H. Qin, H. Cao, S. Qian, Y. Zhao, X. Peng, X. Zhang, X. Liu, P.K. Chu, Synergistic effects of dual Zn/Ag ion implantation in osteogenic activity and antibacterial ability of titanium, Biomaterials 35 (27) (2014) 7699–7713.
- [61] K. Huo, X. Zhang, H. Wang, L. Zhao, X. Liu, P.K. Chu, Osteogenic activity and antibacterial effects on titanium surfaces modified with Zn-incorporated nanotube arrays, Biomaterials 34 (13) (2013) 3467–3478.
- [62] D. Zhu, Y. Su, M.L. Young, J. Ma, Y. Zheng, L. Tang, Biological responses and mechanisms of human bone marrow mesenchymal stem cells to Zn and Mg biomaterials, ACS Appl. Mater. Interfaces 9 (33) (2017) 27453–27461.
- [63] D. Kleiner, The effect of Zn2+ ions on mitochondrial electron transport, Arch. Biochem. Biophys. 165 (1) (1974) 121–125.
- [64] S.L. Sensi, D. Ton-That, P.G. Sullivan, E.A. Jonas, K.R. Gee, L.K. Kaczmarek, J.H. Weiss, Modulation of mitochondrial function by endogenous Zn2+ pools, Proc. Natl. Acad. Sci. U. S. A. 100 (10) (2003) 6157-6162.
- [65] Y.Y. Su, K. Wang, J. Gao, Y. Yang, Y.X. Qin, Y. Zheng, D. Zhu, Enhanced cytocompatibility and antibacterial property of zinc phosphate coating on biodegradable zinc materials, Acta Biomater (2019).
- [66] R. Marsell, T.A. Einhorn, The biology of fracture healing, Injury 42 (6) (2011) 551–555.
- [67] H. Kawamura, A. Ito, S. Miyakawa, P. Layrolle, K. Ojima, N. Ichinose, T. Tateishi, Stimulatory effect of zinc-releasing calcium phosphate implant on bone formation in rabbit femora, J. Biomed. Mater. Res. 50 (2) (2000) 184–190.
- [68] L. Liu, Y. Liu, C. Feng, J. Chang, R. Fu, T. Wu, F. Yu, X. Wang, L. Xia, C. Wu, B. Fang, Lithium-containing biomaterials stimulate bone marrow stromal cell-derived exosomal miR-130a secretion to promote angiogenesis, Biomaterials 192 (2019) 523–536.
- [69] L. Li, X. Peng, Y. Qin, R. Wang, J. Tang, X. Cui, T. Wang, W. Liu, H. Pan, B. Li, Acceleration of bone regeneration by activating Wnt/beta-catenin signalling pathway via lithium released from lithium chloride/calcium phosphate cement in osteoporosis, Sci. Rep. 7 (2017) 45204.
- [70] P. Han, M. Xu, J. Chang, N. Chakravorty, C. Wu, Y. Xiao, Lithium release from β-tricalcium phosphate inducing cementogenic and osteogenic differentiation of both hPDLCs and hBMSCs, Biomater. Sci. 2 (9) (2014).
- [71] Y. Wu, S. Zhu, C. Wu, P. Lu, C. Hu, S. Xiong, J. Chang, B.C. Heng, Y. Xiao, H.W. Ouyang, A bi-lineage conducive scaffold for osteochondral defect regeneration, Adv. Funct. Mater. 24 (28) (2014) 4473–4483.